Supplementary Information

Solar Photons Beyond the Band Gap Wavelengths: Their Effect on Solution-Processed Solar Cells

George Perrakis,[*,a] Apostolos Panagiotopoulos,[b] Temur Maksudov,[c] Chrysa Aivalioti,[c] Essa A. Alharbi,[c,d] Shadi Fatayer,[c] Martin Heeney,[c] Anna C. Tasolamprou,[e] George Kenanakis,[a] Konstantinos Petridis,[f] Thomas D. Anthopoulos,[c,g] S. Ravi P. Silva,[b] Michael Graetzel,[h] Maria Kafesaki,[a,i] and George Kakavelakis[*,f]

Affiliations

[a] Institute of Electronic Structure and Laser (IESL), Foundation for Research and Technology - Hellas (FORTH), 70013 Heraklion, Crete, Greece

[b] Advanced Technology Institute (ATI), Department of Electrical and Electronic Engineering, University of Surrey, Guildford, Surrey GU2 7XH, United Kingdom

[c] KAUST Solar Center (KSC), Physical Sciences and Engineering Division (PSE), King Abdullah University of Science and Technology (KAUST), Thuwal, 23955-6900 Saudi Arabia

[d] Microelectronics and Semiconductor Institute, King Abdulaziz City for Science and Technology (KACST), Riyadh 11442, Saudi Arabia

[e] Department of Physics, National and Kapodistrian University of Athens, 15784, Athens, Greece

[f] Department of Electronic Engineering, School of Engineering, Hellenic Mediterranean University, Romanou 3, Chalepa, Chania, Crete GR-73100, Greece

[g] Henry Royce Institute and Photon Science Institute, Department of Electrical and Electronic Engineering, The University of Manchester, Oxford Road, Manchester M13 9PL, United Kingdom

[h] Laboratory of Photonics and Interfaces, Institute of Chemical Sciences and Engineering, Ecole Polytechnique Federal de Lausanne, Lausanne 1015, Switzerland

[i] Department of Materials Science and Engineering, University of Crete, 70013 Heraklion, Crete, Greece

*Corresponding author email: gperrakis@iesl.forth.gr; kakavelakis@hmu.gr

In the Supplementary Information, we provide additional theoretical and experimental details, including stacks' layout, temperature coefficients of power conversion efficiency, environmental conditions, and transparent conductive oxides' complex refractive indices, and supplementary figures, including parametric analysis, comparable study with silicon technology, evaluation of heating/cooling load, and investigation of various effects, including thin-film interference and expanded band tail states. The document includes, 12 sections, 24 pages and 15 figures:

S1. Stack layout and cross-sectional scanning electron microscopy (SEM) images of fabricated/examined single-junction organic (OSC), perovskite (PSC), and tandem OSC/PSC, PSC/PSC solution-processed solar cells (SSCs)

S2. SSCs' temperature coefficients of power conversion efficiency (β_{PCE})

S3. Parametric analysis

S4. Actual environmental conditions

S5. Physical origin of increasing conversion losses and T with λ_g

S6. Complex refractive indices of the transparent conductive oxides (TCOs) in 300–2500 nm

S7. Investigation of thin-film interference effects in SSCs in λ_g–2500 nm

S8. Physical origin of heat source and its dependence on device architecture and λ_g

S9. Physical origin of radiative cooling load and its potential in SSCs

S10. Investigation of the effect of expanded band tail states in perovskites on PSCs' optical properties and operation

S11. Comparable study on optical properties and operation for conventional (silicon) wafer-scaled solar cells and SSCs

S12. Physical behavior of SSCs during noontime in November

S1. Stack layout and cross-sectional scanning electron microscopy (SEM) images of fabricated/examined single-junction organic (OSC), perovskite (PSC), and tandem OSC/PSC, PSC/PSC solution-processed solar cells (SSCs)

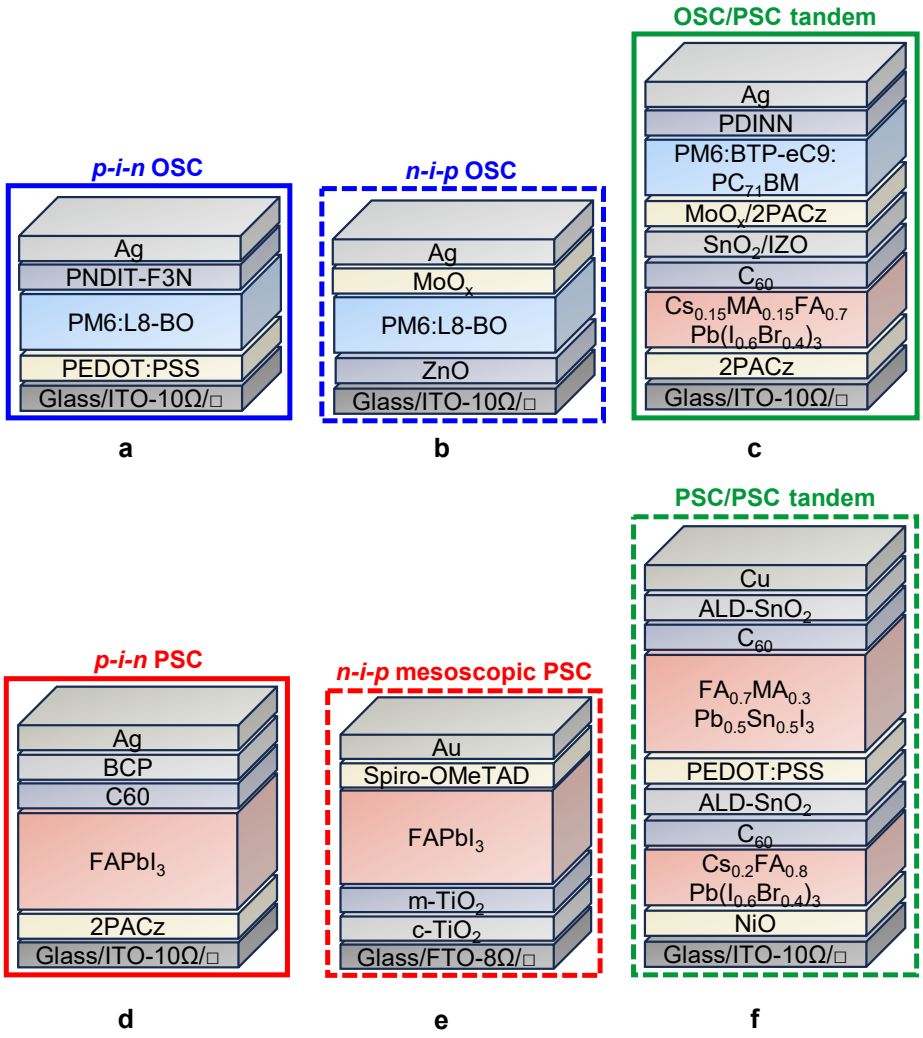

Fig. S1 Stack layout of fabricated (a) *p-i-n* OSC (blue), (b) *n-i-p* OSC (dashed blue), (c) OSC/PSC (green), (d) *p-i-n* PSC (red), (e) *n-i-p* mesoscopic PSC (dashed red), and (f) PSC/PSC (dashed green) composed of various hole-transport layers (PEDOT:PSS, 2PACz, MoO_x, NiO, and Spiro-OMeTAD), electron-transport layers (TiO_2, SnO_2, ZnO, PNDIT-F3N, C_{60}/BCP, and PDINN), transparent conductive oxides (ITO and FTO), metal contacts (Ag, Au, and Cu), and active layers (PM6:L8-BO, PM6:BTP-eC9:$PC_{71}BM$, $Cs_{0.15}MA_{0.15}FA_{0.7}Pb(I_{0.6}Br_{0.4})_3$, $FAPbI_3$, $Cs_{0.2}FA_{0.6}Pb(I_{0.6}Br_{0.4})_3$, and $FA_{0.7}MA_{0.3}Pb_{0.5}Sn_{0.5}I_3$).

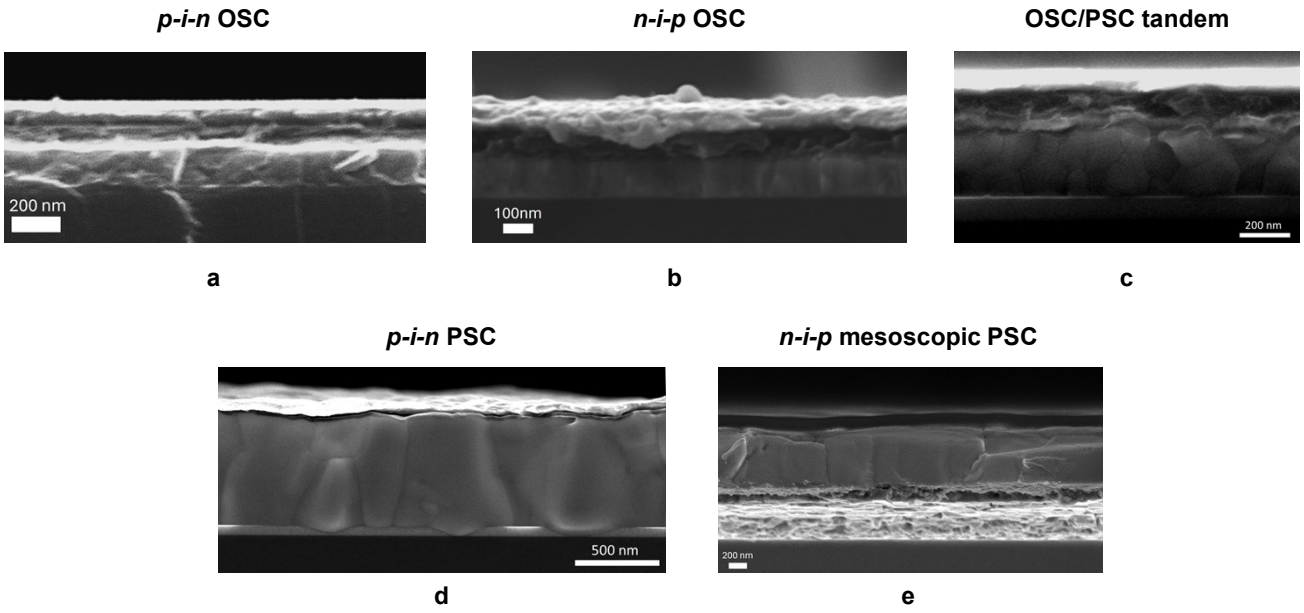

Fig. S2 Scanning electron microscopy (SEM) cross-sectional images of fabricated SSCs: (a) *p-i-n* OSC, (b) *n-i-p* OSC, (c) OSC/PSC, (d) *p-i-n* PSC, and (e) *n-i-p* mesoscopic PSC. Note that the cross-sectional SEM images of fabricated SSCs appear also in the main manuscript as insets in Figure 1, added in the Supplementary Information at a larger scale for better clarity.

S2. SSCs' temperature coefficients of power conversion efficiency (β_{PCE})

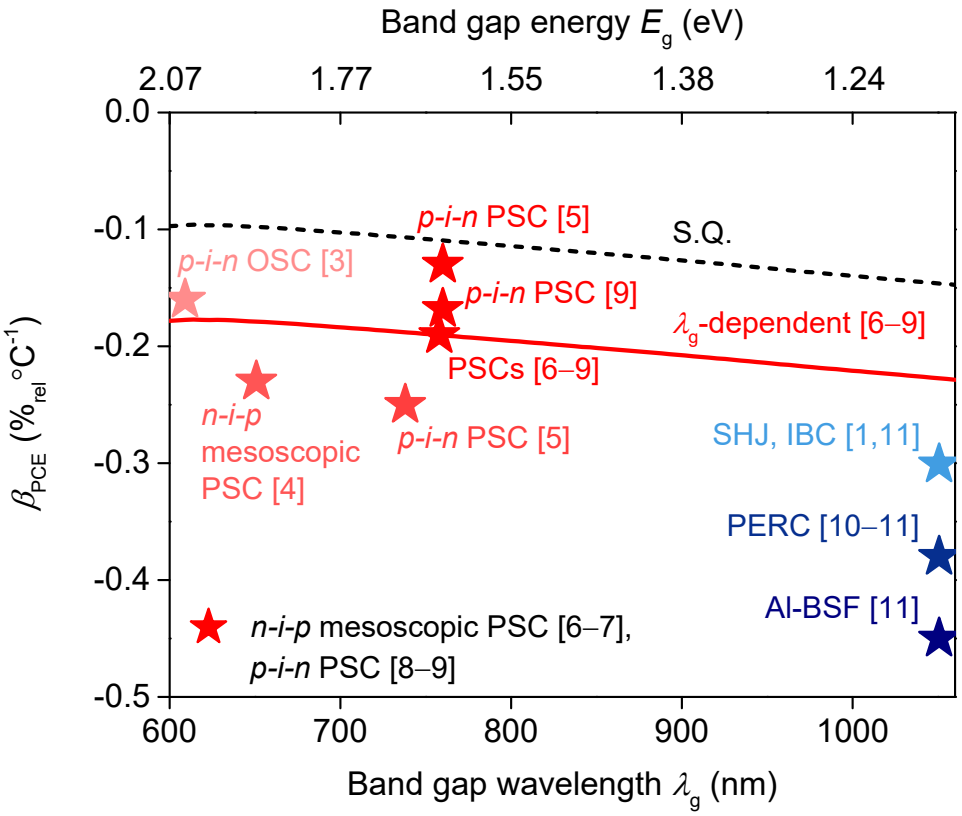

Fig. S3 Temperature coefficient of power conversion efficiency (β_{PCE}), i.e., slopes of the PCE (%)−T_c curves, where T_c is the cell temperature, as a function of band gap wavelength (λ_g) or band gap energy (E_g). β_{PCE} is normalized at % compared to the solar cells operating at Standard Test Conditions (STC) (i.e., 1000 W/m^2 of solar radiation, T_c = 25°C). The black dashed curve corresponds to β_{PCE} calculated based on the detailed balance method described by Shockley and Queisser (SQ) assuming ideal (and electrically homogeneous) solar cells.[1,2] Red stars correspond to experimental β_{PCE} of SSCs in the literature.[3–9] The red solid curve indicates the λ_g-dependent SQ β_{PCE} shifted to experimental β_{PCE} values of fabricated PSCs in the literature.[6–9] Blue stars correspond to experimental β_{PCE} of current industrial (silicon) passivated emitter and rear cells (PERC),[10,11] with interdigitated back contacts (IBC),[1] aluminum back surface field (Al-BSF),[11] and silicon heterojunction solar cells (SHJ)[11] plotted for reference.

S3. Parametric analysis

We perform a parametric analysis on SCCs' PCE loss relative to STC (ΔPCE($\%_{rel,STC}$)) and operating temperature (T), to examine the interplay of parasitic absorption (~300–2500 nm) and conversion losses (<λ_g) on SSCs' operation as well as the physical origin of conversion losses. Specifically, we calculate ΔPCE($\%_{rel,STC}$) (Figure S4c–d) and operating or steady-state temperature (T) (Figure S4a–b) by solving eq 1 of the main text (see Experimental/Theoretical Methods) as a function of (i) λ_g (or E_g), (ii) PCE in STC (PCE_{STC}), and (iii) sub-band gap absorption above λ_g up to 2500 nm. For the calculations, we assume 100% absorption of photons below λ_g, 0% (Figure S4a,c), and 35% (Figure S4b,d) of sub-band gap absorption above λ_g, i.e., based on the experimental absorptance spectra of fabricated SCCs in λ_g–2500 nm, see Figure 1a–f. Moreover, we used realistic β_{PCE}, as calculated in Figure S2 (red curve), and environmental conditions, i.e., 25°C ambient temperature, 50% relative humidity (see Figure S5d), 2.5 m/s wind speed (~16.5 W/m^2/°C), and AM1.5G. In Figure S4a–d, y-axis limits are determined by SQ limit for single-junction solar cells and realistic/empirical limit for tandem SSCs.[12] We also plot for reference λ_g and PCE_{STC} of experimental PSCs (i.e., CsFAPbIBr-,[13] $MAPbI_3$-,[14] $FAPbI_3$-,[15] and $FAMAPbSnI_3$-based PSCs[13]), OSCs (i.e., P3HT:PCBM-,[16] PTB7-Th:$PC_{71}BM$-,[17] PM6:BTP-eC9:PCBM-,[18] and PM6:L8-BO-based OSCs[19]), and their tandems (T) (i.e., PM6:BTP-eC9:PCBM-based OSC/PSC,[18] and $FAMAPbSnI_3$-based PSC/PSC[13]), see red, blue, and green rhombuses in Figure S4a–d, respectively.

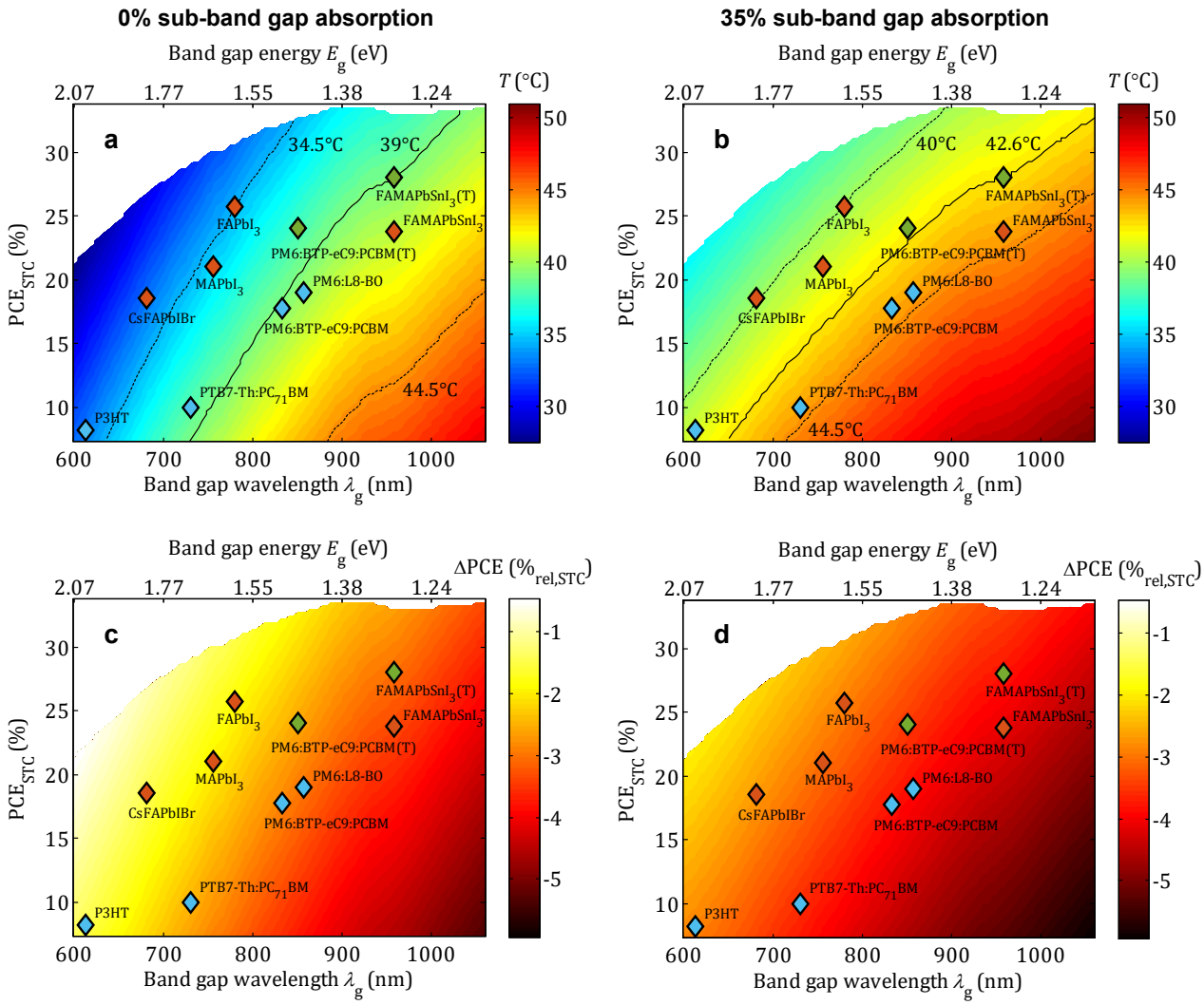

Fig. S4 Impact of varying λ_g (or E_g) and PCE in STC (PCE$_{STC}$) on (a–b) operating or steady-state temperature (T) and (c–d) PCE loss relative to STC (ΔPCE(%$_{rel,STC}$)) (see eqs 1 and 6 – Experimental/Theoretical Methods), assuming (a–d) 100% absorption of photons below λ_g, (a,c) 0%, and (b,d) 35% of sub-band gap absorption above λ_g up to 2500 nm, i.e., based on the experimental absorptance spectra of fabricated SCCs in λ_g–2500 nm shown in Figure 1a–f. For calculations in (a–d), we used realistic β_{PCE}, as calculated in Figure S2 (red curve), and environmental conditions, i.e., 25°C ambient temperature, 50% relative humidity (see Figure S5d), 2.5 m/s wind speed (~16.5 W/m^2/°C), and AM1.5G. In (a–d), y-axis limits are determined by SQ limit for single-junction solar cells and realistic/empirical limit for tandem SSCs.[12] Red, blue, and green rhombuses correspond to λ_g and PCE$_{STC}$ of experimental PSCs (i.e., CsFAPbIBr-,[13] MAPbI$_3$-,[14] FAPbI$_3$-,[15] and FAMAPbSnI$_3$-based PSCs[13]), OSCs (i.e., P3HT:PCBM-,[16] PTB7-

Th:$PC_{71}BM$-,[17] PM6:BTP-eC9:PCBM-,[18] and PM6:L8-BO-based OSCs[19]), and their tandems (T) (i.e., PM6:BTP-eC9:PCBM-based OSC/PSC,[18] and $FAMAPbSnI_3$-based PSC/PSC[13]) plotted for reference.

As shown in Figure S4a, SSCs (rhombuses) can reach high operating temperatures up to ~40.5°C if λ_g and PCE_{STC} are not carefully optimized (see $FAMAPbSnI_3$-based PSC), with a temperature variance up to ~7.4°C (see P3HT:PCBM-based OSC versus $FAMAPbSnI_3$-based PSC). Due to the negative θ_{PCE} (see Figure S2), PCE decreases as T increases, leading up to $\Delta PCE(\%_{rel,STC})$ ~ -3.3%$_{rel}$ (see $FAMAPbSnI_3$-based PSC in Figure S4c), and $\Delta PCE(\%_{rel,STC})$ variance up to ~2.0%$_{rel}$ (see CsFAPbIBr-based PSC versus $FAMAPbSnI_3$-based PSC in Figure S4c).

Operating temperature can be even higher up to ~44.1°C (see $FAMAPbSnI_3$-based PSC in Figure S4b) for 35% of sub-band gap absorption (>λ_g), leading up to $\Delta PCE(\%_{rel,STC})$ ~ -4.1%$_{rel}$ (see $FAMAPbSnI_3$-based PSC in Figure S4d). Interestingly, temperature variance decreases as sub-band gap absorption increases, ~2.9°C (see P3HT:PCBM-based OSC versus $FAMAPbSnI_3$-based PSC in Figure S4b), hence $\Delta PCE(\%_{rel,STC})$ variance, ~1.4%$_{rel}$ (see CsFAPbIBr-based PSC versus $FAMAPbSnI_3$-based PSC in Figure S4d).

These results (Figure S4a–d) indicate that as parasitic absorption increases the operating temperature (hence $\Delta PCE(\%_{rel,STC})$) of SSCs of lower λ_g increases with higher rate than that of SSCs of higher λ_g (see Figure S4a versus 4b). The reason is the similar parasitic absorption in SSCs in λ_g–2500 nm no matter functional materials (see Figure 2). Consequently, higher parasitic heat source is expected for SSCs with lower λ_g, which increases T and PCE loss, due to the higher solar irradiance at lower wavelengths (see Figure 1a – yellow). In contrast, SSCs of higher λ_g including tandems despite their even higher PCE_{STC} (see $FAMAPbSnI_3$-based PSC/PSC versus $FAMAPbSnI_3$-based PSC) are bound to operate at higher device temperatures (hence higher PCE losses) than SSCs of lower λ_g (see $FAPbI_3$-based PSC versus $FAMAPbSnI_3$-based PSC/PSC). Results in Figure S4a–b reveal that this effect arises from conversion losses of fundamental nature due to the less efficient spectrum utilization as λ_g increases rather than being architecture constrained, i.e., due to unoptimized PCE_{STC}. Specifically, for experimental SSCs (rhombuses), T is predominantly affected by λ_g (x-axis) rather than PCE_{STC} (y-axis); see also Figure S6 showing the physical origin of increasing T with λ_g. Consequently, results in Figure S4 show an opposing effect of parasitic

sub-band gap absorption (λ_g–2500 nm) and conversion losses (~300–λ_g nm) on *T* with respect to λ_g. Due to this opposing effect, all SSCs (no matter architectures, TCOs, functional/transport materials, active layers, or λ_g) are expected to operate not only at higher but also similar temperatures (hence similar PCE loss) as sub-band gap absorption increases or (equivalently) in the absence of thermal management.

S4. Actual environmental conditions

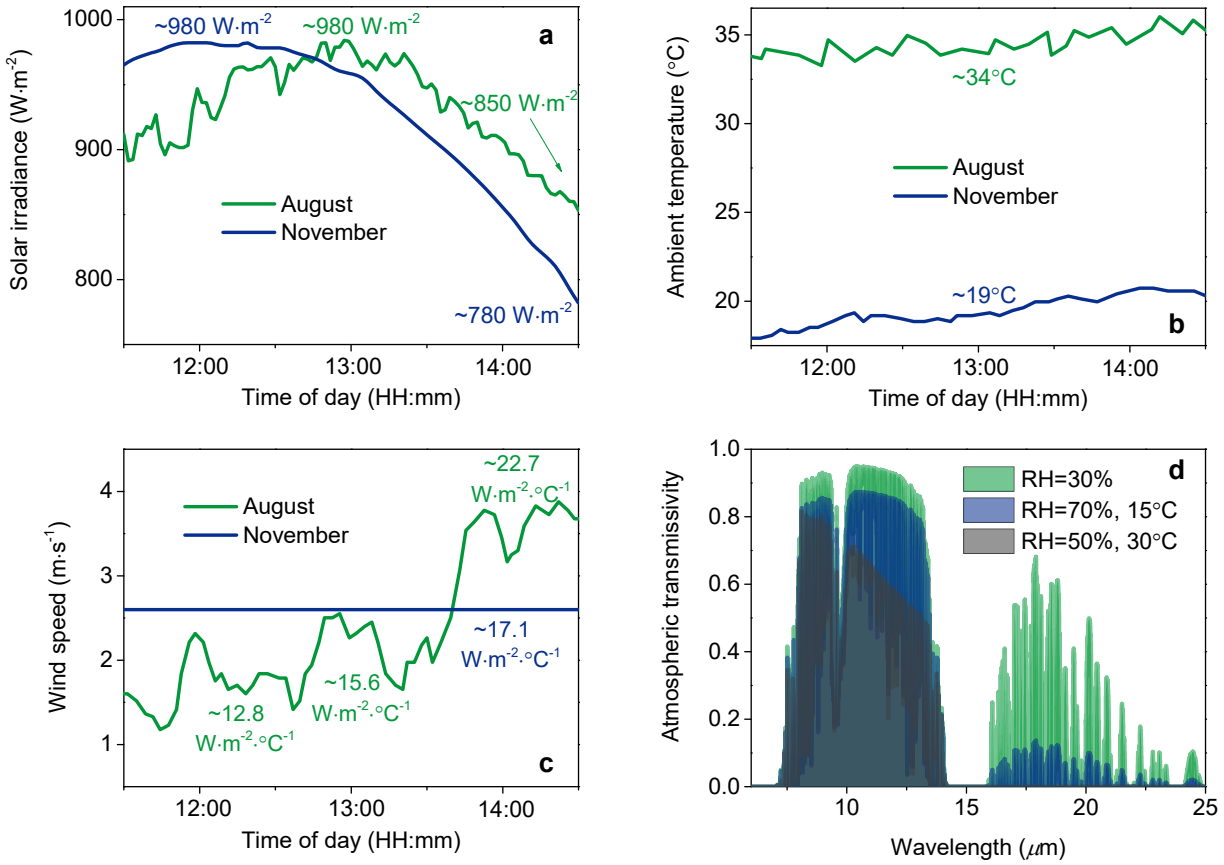

Fig. S5 Time-dependent (a) solar irradiance, (b) ambient temperature, (c) wind speed, and (d) atmospheric transmissivity depending on relative humidity and ambient temperature, during noontime a day in August (green) and November (blue) extracted from actual environment situations.[10,20–22] Values in (c) indicate the calculated wind-speed-dependent nonradiative heat transfer coefficients (see Experimental/Theoretical Methods).

S5. Physical origin of increasing conversion losses and T with λ_g

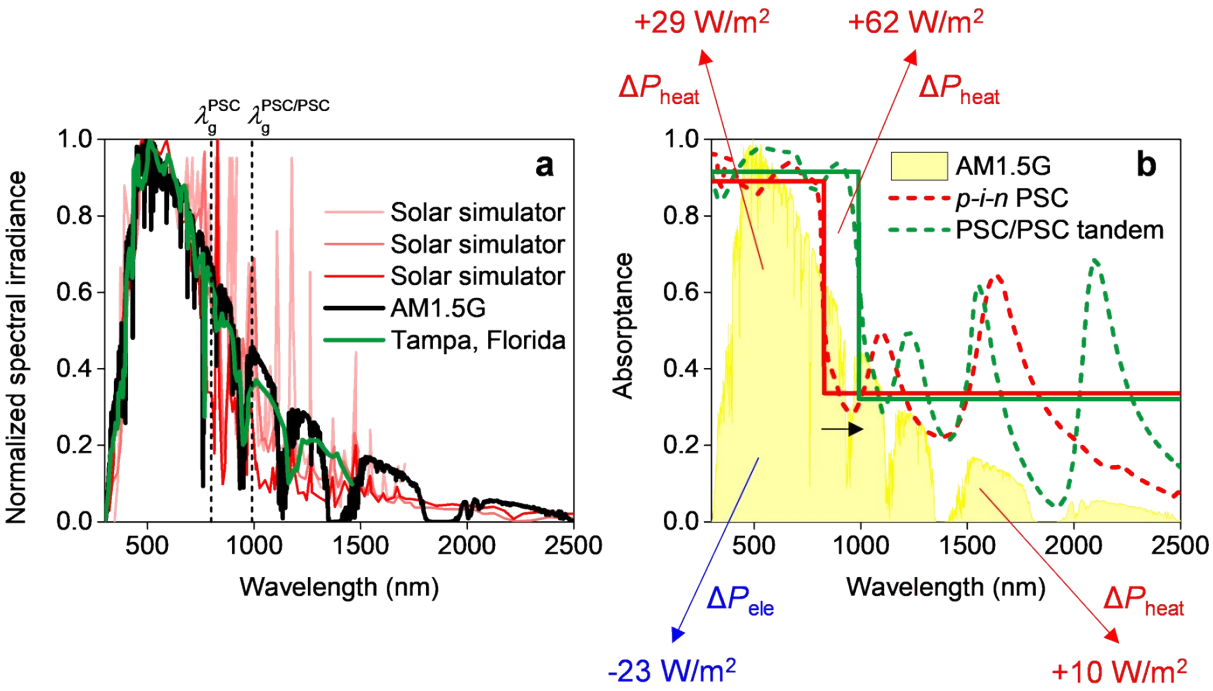

Fig. S6 (a) Normalized spectral irradiance of solar simulators' (red)[23–25] compared to actual measurements, i.e., Tampa, Florida (green)[26] and standard AM1.5G spectrum (black). (b) Measured (dashed) versus mean (solid) absorptance spectra in 300–2500 nm for examined PSC/PSC and *p-i-n* PSC, together with the normalized AM1.5G solar irradiance spectra (yellow). Red arrows indicate the increased heat source in PSC/PSC compared to *p-i-n* PSC in each spectral regime calculated from $\Delta P_{heat} = \int_{\lambda_1}^{\lambda_2} \alpha_{PSC/PSC}(\lambda) I_{AM1.5G}(\lambda) d\lambda - \int_{\lambda_1}^{\lambda_2} a_{PSC}(\lambda) I_{AM1.5G}(\lambda) d\lambda$, where $\alpha(\lambda)$ is the measured absorptance of each SSC and $I_{AM1.5G}(\lambda)$ is the solar illumination represented by AM1.5G. Blue arrow indicates the lower electricity output power in *p-i-n* PSC compared to PSC/PSC calculated from $\Delta P_{ele} = G \cdot PCE_{STC}^{PSC}/100 - G \cdot PCE_{STC}^{PSC/PSC}/100$, where G = 1000 W/m² is the integrated AM1.5G spectral irradiance. ΔP_{ele} in the case of PSC/PSC does not overwhelm ΔP_{heat} in $\lambda_g^{PSC} - \lambda_g^{PSC/PSC}$.

S6. Complex refractive indices of the transparent conductive oxides (TCOs) in 300–2500 nm

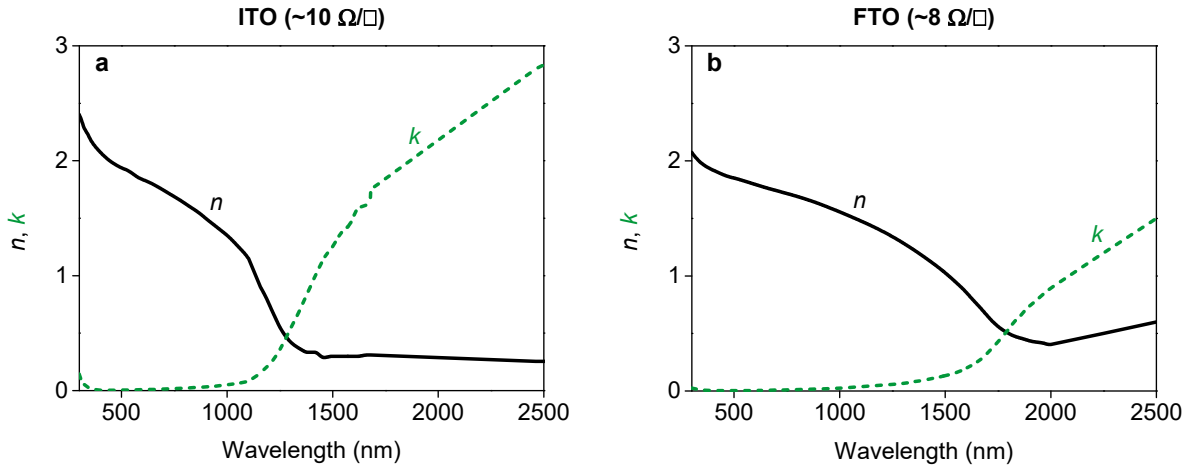

Fig. S7 Refractive index (*n* – black) and extinction coefficient (*k* – green) of (a) indium tin oxide (ITO) and (b) fluorine-doped tin oxide (FTO) transparent conductive oxides used for simulating the absorption properties of fabricated SSCs in 300–2500 nm (Figure 1a–f) extracted from refs [27–29] and [30–32] for ITO and FTO, respectively.

S7. Investigation of thin-film interference effects in SSCs in λ_g–2500 nm

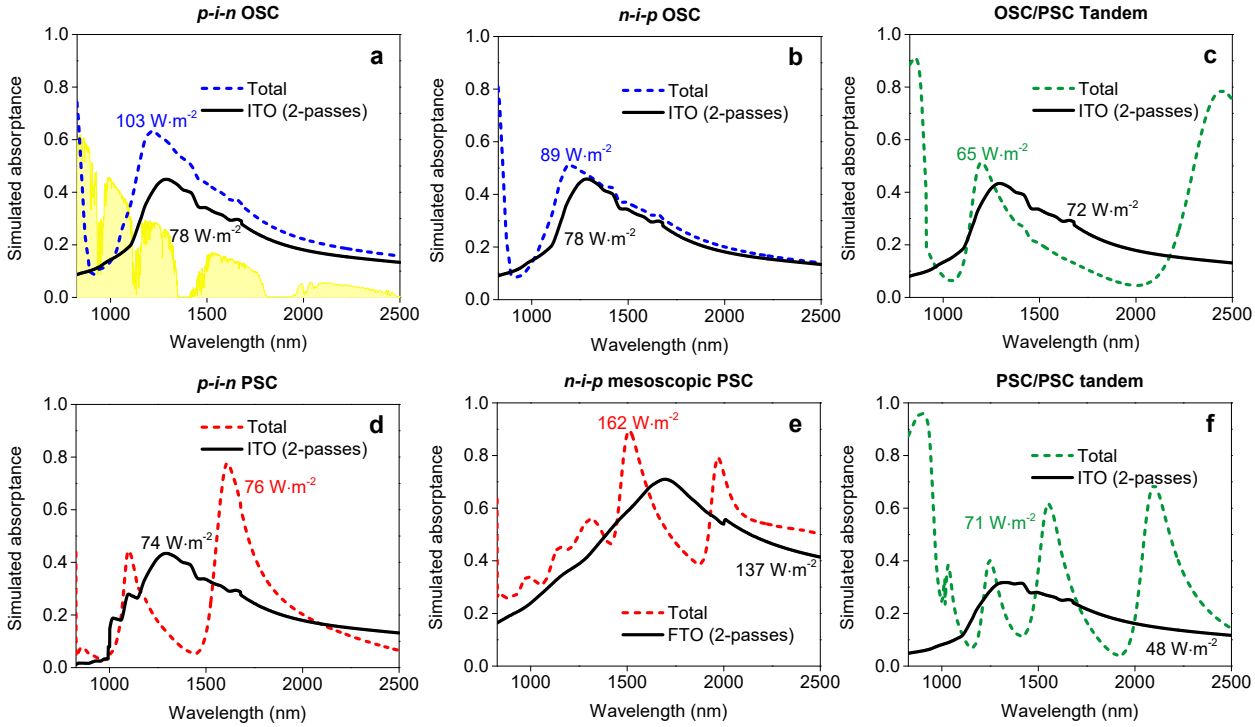

Fig. S8 Simulated total (dashed) and 2-pass (solid) absorptance spectra in 830–2500 nm of examined (a) *p-i-n* OSC (blue), (b) *n-i-p* OSC (blue), (c) OSC/PSC (green), (d) *p-i-n* PSC (red), (e) *n-i-p* mesoscopic PSC (blue), and (f) PSC/PSC (green), together with the AM 1.5G solar irradiance spectra (plotted only in (a) for clarity). Values in (a–f) indicate parasitic heat source in λ_g–2500 nm, where λ_g ~ 900, 910, 830, and 1020 nm for OSCs, OSC/PSC, PSCs, and PSC/PSC, respectively, calculated based on the simulated absorptance (a–f) and AM1.5G (a) (see eq 6 for PCE=0 (Experimental/Theoretical Methods)).

S8. Physical origin of heat source and its dependence on device architecture and λ_g

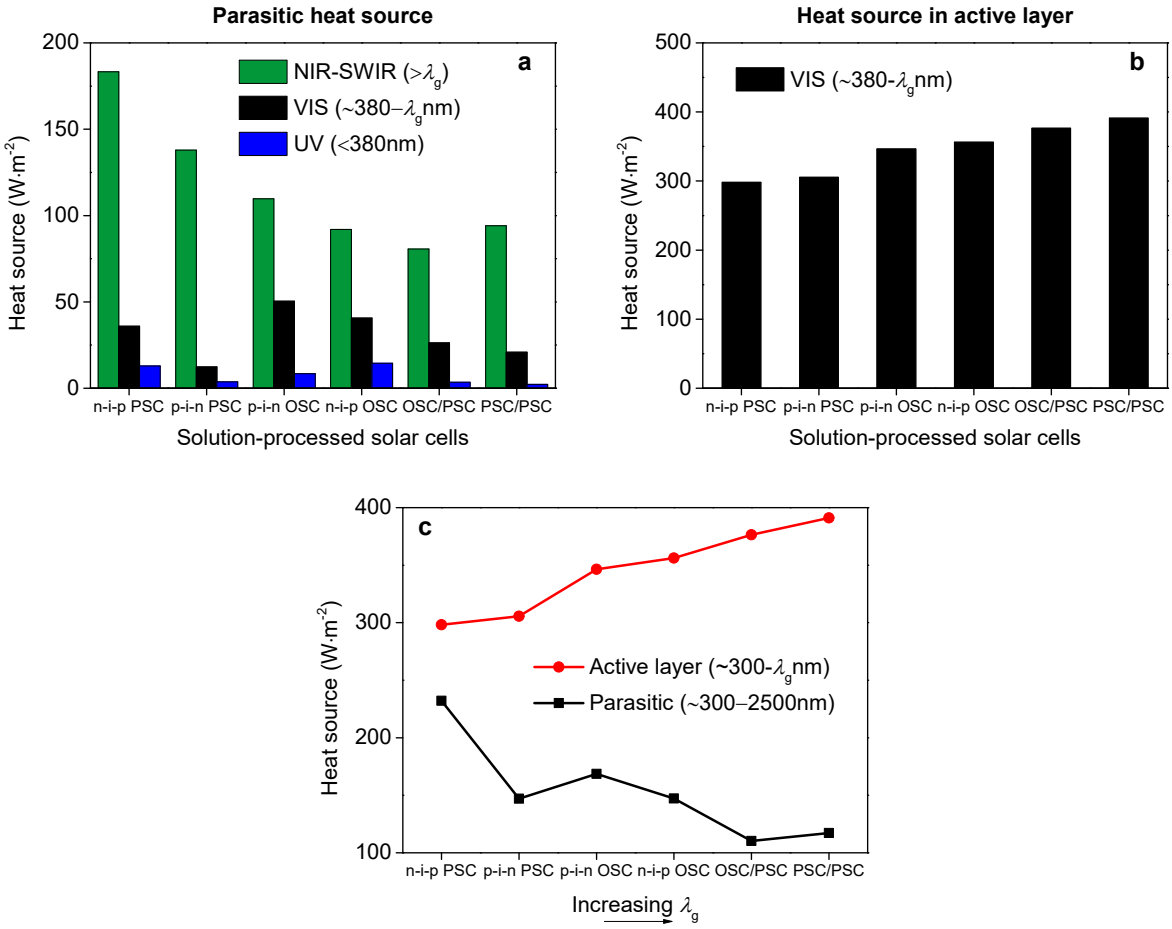

Fig. S9 (a) Parasitic heat source in fabricated SSCs (see Figure 1a–f – insets) in >λ_g (NIR-SWIR – green), ~380–λ_g nm (VIS – black), and <380 nm (UV – blue) calculated from eq 6 for PCE=0 (see Experimental/Theoretical Methods) based on the experimental absorptance (see Figure 1a–f – solid) and AM1.5G (Figure 1a). (b) Heat source in SSCs' active layer calculated from eq 6 (see Experimental/Theoretical Methods) based on the simulated absorption in active layer (see Figure 1a–f – dashed), simulated parasitic absorption (see Figure 2a–f), and AM1.5G (see Figure 1a). (c) Dependence of heat source in active layer (red) and parasitic heat source in 300–2500 nm (black) on λ_g.

S9. Physical origin of radiative cooling load and its potential in SSCs

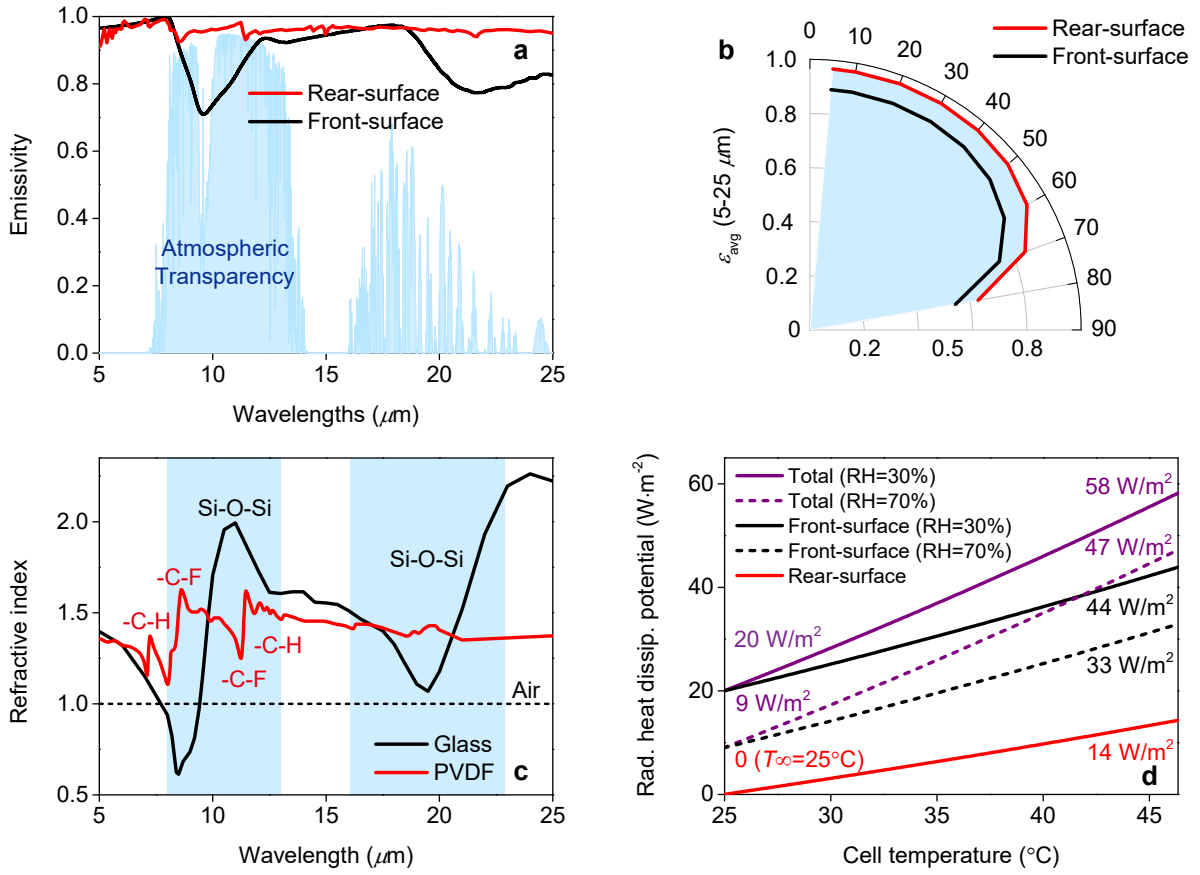

Fig. S10 (a) Measured front- (black) and rear-surface (red) emissivity of SSCs, together with the infrared transmission of the atmosphere (blue). Front-surface emissivity was obtained from measuring the reflectance and transmittance of fabricated SSCs' front surface in MIR (>4 μm) (see Experimental/Theoretical Methods). Rear-surface emissivity was extracted from refs [33,34] assuming highly-emissive encapsulation with typical encapsulant PVDF. (b) Polar distribution of the average front- (black) and rear-surface emissivity (red) across 5–25 μm (i.e., also within the atmospheric transparency window, 8–13 μm) at different angles from 10° to 80°. (c) Refractive index of glass substrate (black solid curve) and PVDF encapsulant (red solid curve) obtained from refs [34,35], showing the origin of SSCs' front- and rear-surface emissivity dips in (a). Specifically, SSCs' reflectivity increases in >4 μm mainly due to reflection from the front-surface, decreasing SSCs' emissivity, hence radiative cooling potential in MIR, due to strong impedance mismatch between glass (black solid curve) and air (black dashed line) arising from glass

phonon-polariton resonance due to vibrational absorptions in MIR.[1,33,36] (d) Front-surface (black), rear-surface (red), and total (purple) radiative heat dissipation potential as a function of cell temperature (T_c) and relative humidity (see Figure S5d),[37] calculated from eqs 2–4 (see Experimental/Theoretical Methods) based on SSCs' front-surface (black), rear-surface (red) emissivity shown in (a–b) and ideal emissivity~1, respectively.

S10. Investigation of the effect of expanded band tail states in perovskites on PSCs' optical properties and operation

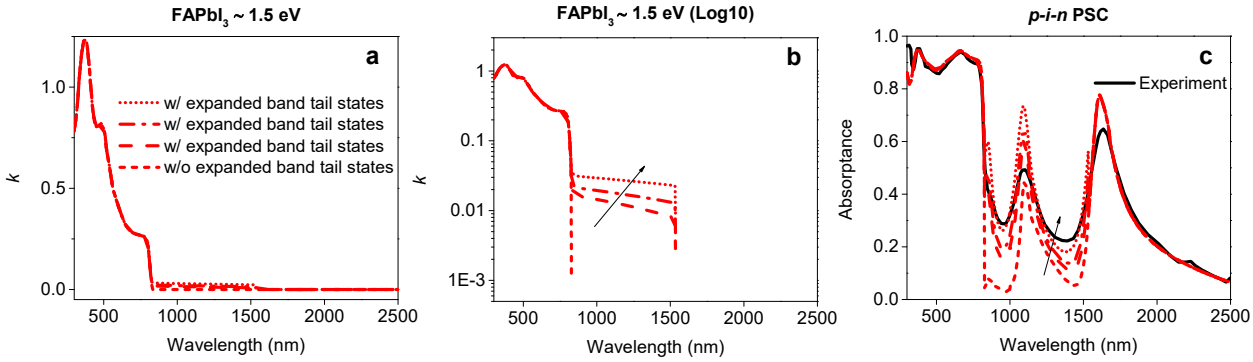

Fig. S11 Investigation of the effect of expanded band tail states in perovskites on (a–b) $FAPbI_3$ extinction coefficient (k) and (c) *p-i-n* PSCs' absorptance. Black arrows indicate gradual increase of PSC absorptance at $>\lambda_g$ due to gradual increase of k at $>\lambda_g$.

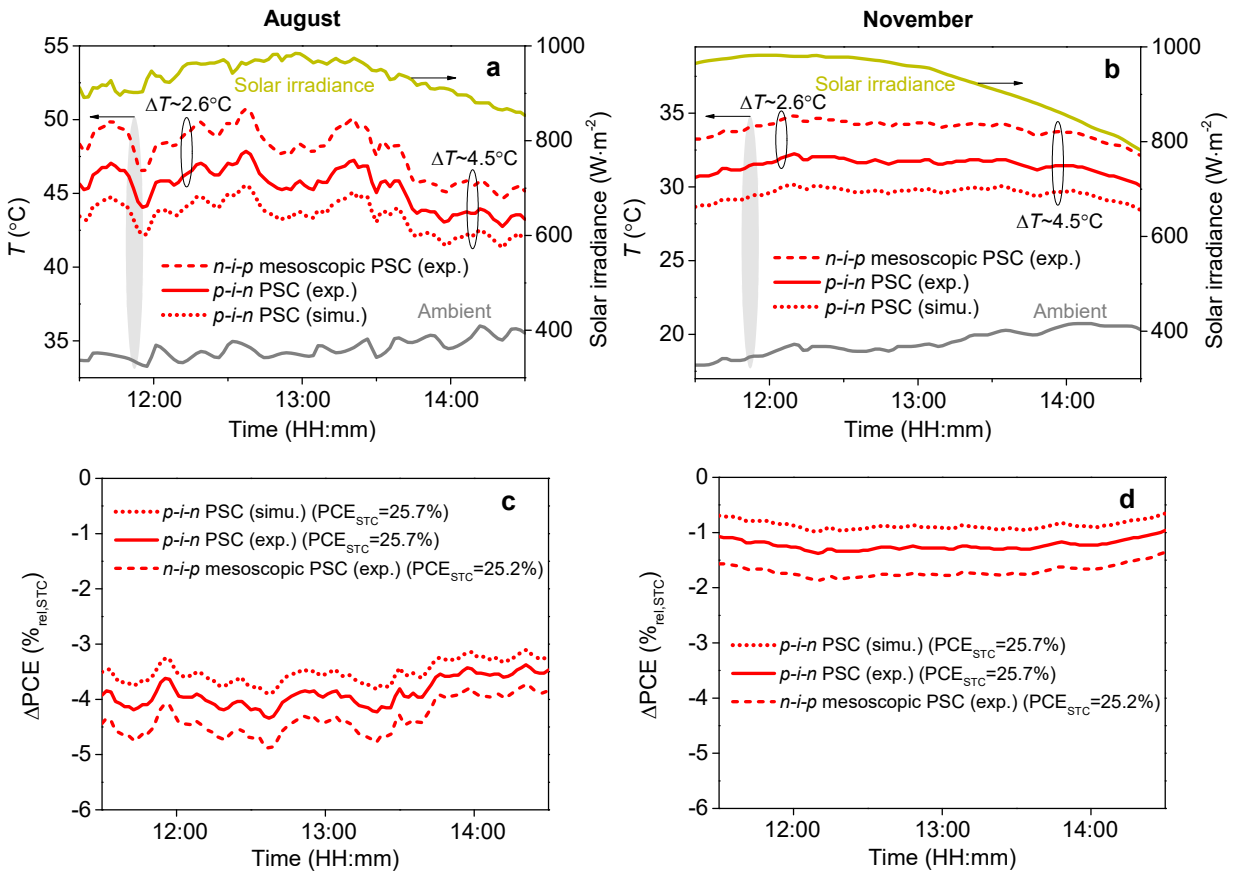

Fig. S12 Simulated time-dependent outdoor performance under real world conditions during a day in August (a,c) and November (b,d), indicating (a–b) temperature and (c–d) PCE losses reduction in the absence of expanded band tail states in perovskites (dotted red line – see also Figure S11) on *p-i-n* PSC operation. (a–b) Time-dependent *T* and (c–d) ΔPCE($\%_{rel,STC}$) for experimental *n-i-p* mesoscopic PSC (red dashed), experimental *p-i-n* PSC (red solid), and simulated *p-i-n* PSC (red dotted) shown in Figures 1e, 1d (solid), and 1d (dashed), respectively. The time-dependent performance of SSCs is investigated by combining the experimental data of solar irradiance (yellow), ambient air temperature (gray), wind speed (Figure S5c), and relative humidity (Figure S5d).[10,20–22]

S11. Comparable study on optical properties and operation for conventional (silicon) wafer-scaled solar cells and SSCs

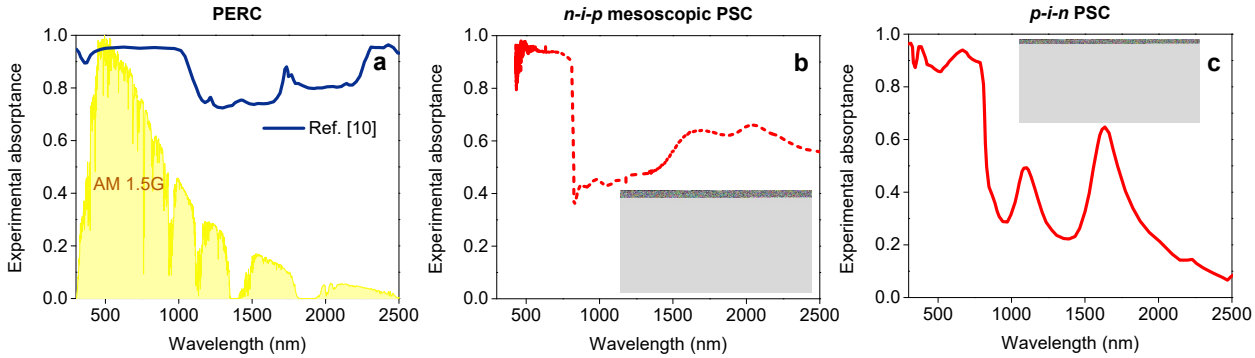

Fig. S13 Experimental absorptance spectra in 300–2500 nm, top photo, and scanning electron microscopy (SEM) cross-sectional images (insets) of (a) current industrial (silicon) passivated emitter and rear cells (PERC) extracted from ref [10] (blue) and (b–c) fabricated *n-i-p* mesoscopic (red dashed) and *p-i-n* (red solid) PSCs, respectively, together with the AM 1.5G solar irradiance spectra (plotted only in (a) for clarity).

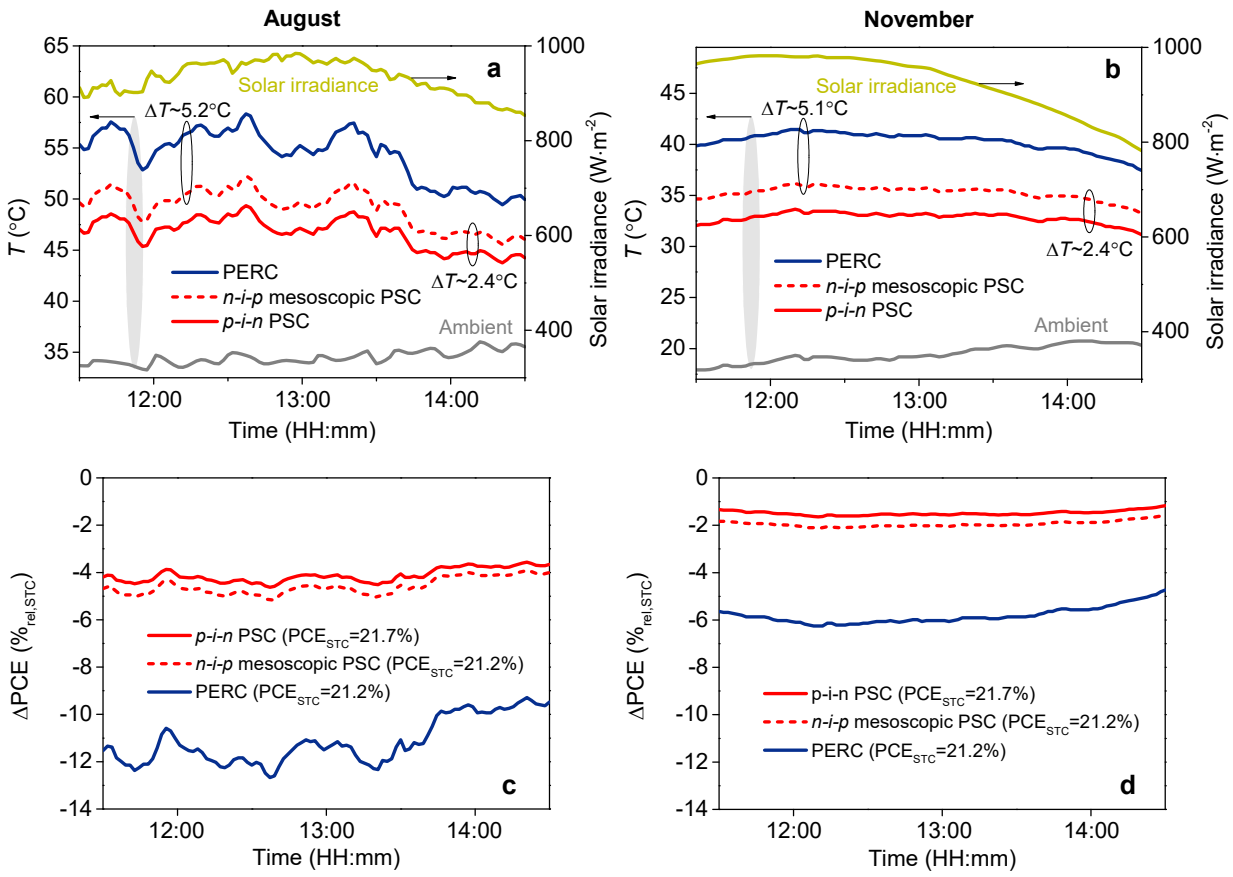

Fig. S14 Simulated time-dependent outdoor performance under real world conditions during a day in August (a,c) and November (b,d), comparing SSCs' performance with conventional (silicon) technology. (a–b) Time-dependent *T* and (c–d) ΔPCE($\%_{rel,STC}$) for PERC (blue), *n-i-p* mesoscopic PSC (red solid), and *p-i-n* PSC (red dotted) shown in Figures S13a, 1e (solid), and 1d (solid), respectively. The time-dependent performance of SSCs is investigated by combining the experimental data of solar irradiance (yellow), ambient air temperature (gray), wind speed (Figure S5c), and relative humidity (Figure S5d).[10,20–22]

S12. Physical behavior of SSCs during noontime in November

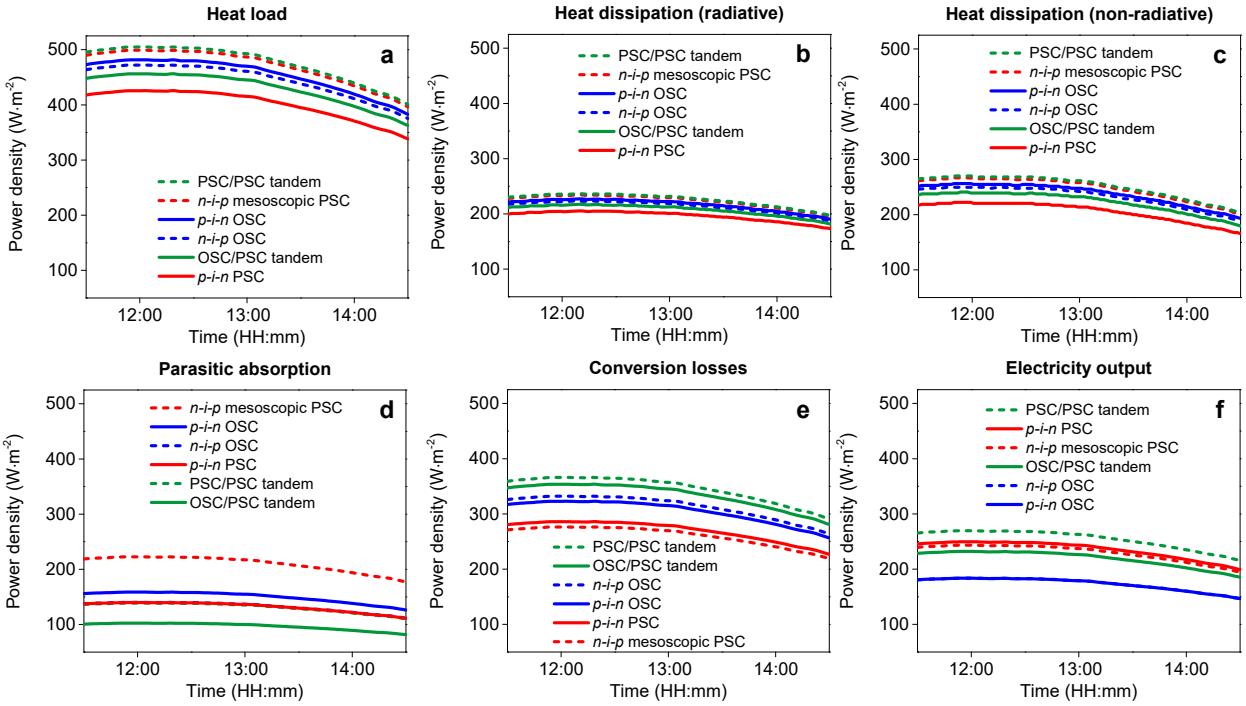

Fig. S15 Simulated time-dependent (a) heat load, (b) radiative and (c) non-radiative heat dissipation, (d) parasitic absorption, (e) conversion losses, and (f) electricity output of fabricated *p-i-n* OSC (blue solid), *n-i-p* OSC (blue dashed), OSC/PSC (green solid), *p-i-n* PSC (red solid), *n-i-p* mesoscopic PSC (red dashed), and PSC/PSC (green dashed) operating under real world conditions during a day in November. The time-dependent performance of SSCs is investigated by combining the experimental data of solar irradiance (Figure S5a), ambient air temperature (Figure S5b), wind speed (Figure S5c), and relative humidity (Figure S5d).[20,37]

References

1 G. Perrakis, A. C. Tasolamprou, G. Kenanakis, E. N. Economou, S. Tzortzakis and M. Kafesaki, *Opt Express*, 2020, **28**, 18548.

2 W. Shockley and H. J. Queisser, *J Appl Phys*, 1961, **32**, 510–519.

3 G. Bardizza, E. Salis, C. Toledo and E. D. Dunlop, *Progress in Photovoltaics: Research and Applications*, 2020, **28**, 593–600.

4 Z. Dong, W. Li, H. Wang, X. Jiang, H. Liu, L. Zhu and H. Chen, *Solar RRL*, 2021, **5**, 2100370.

5 T. Moot, J. B. Patel, G. McAndrews, E. J. Wolf, D. Morales, I. E. Gould, B. A. Rosales, C. C. Boyd, L. M. Wheeler, P. A. Parilla, S. W. Johnston, L. T. Schelhas, M. D. McGehee and J. M. Luther, *ACS Energy Lett*, 2021, **6**, 2038–2047.

6 S. Pescetelli, A. Agresti, G. ✉ Viskadouros, G. Viskadouros, S. Razza, K. Rogdakis, I. Kalogerakis, E. Spiliarotis, E. Leonardi, P. Mariani, L. Sorbello, M. Pierro, C. Cornaro, S. Bellani, L. Najafi, B. Martín-García, A. Esaú, D. R. Castillo, R. Oropesa-Nuñez, M. Prato, S. Maranghi, M. L. Parisi, A. Sinicropi, R. Basosi, F. Bonaccorso, E. Kymakis and A. Di Carlo, *Nature Energy 2022*, 2022, 1–11.

7 W. Tress, K. Domanski, B. Carlsen, A. Agarwalla, E. A. Alharbi, M. Graetzel and A. Hagfeldt, *Nature Energy 2019 4:7*, 2019, **4**, 568–574.

8 Z. Wei, J. He, Y. Shi, Q. Li, Q. Niu, Y. Hou and S. Yang, *Solar Energy*, 2023, **264**, 112040.

9 M. Jošt, B. Lipovšek, B. Glažar, A. Al-Ashouri, K. Brecl, G. Matič, A. Magomedov, V. Getautis, M. Topič and S. Albrecht, *Adv Energy Mater*, 2020, **10**, 2000454.

10 Z. Li, S. Ahmed and T. Ma, *Solar RRL*, 2021, **5**, 2000735.

11 J. Haschke, J. P. Seif, Y. Riesen, A. Tomasi, J. Cattin, L. Tous, P. Choulat, M. Aleman, E. Cornagliotti, A. Uruena, R. Russell, F. Duerinckx, J. Champliaud, J. Levrat, A. A. Abdallah, B. Aïssa, N. Tabet, N. Wyrsch, M. Despeisse, J. Szlufcik, S. De Wolf and C. Ballif, *Energy Environ Sci*, 2017, **10**, 1196–1206.

12 M. Jošt, L. Kegelmann, L. Korte and S. Albrecht, *Adv Energy Mater*, 2020, **10**, 1904102.

13 R. Lin, Y. Wang, Q. Lu, B. Tang, J. Li, H. Gao, Y. Gao, H. Li, C. Ding, J. Wen, P. Wu, C. Liu, S. Zhao, K. Xiao, Z. Liu, C. Ma, Y. Deng, L. Li, F. Fan and H. Tan, *Nature 2023 620:7976*, 2023, **620**, 994–1000.

14 Z. Chen, B. Turedi, A. Y. Alsalloum, C. Yang, X. Zheng, I. Gereige, A. Alsaggaf, O. F. Mohammed and O. M. Bakr, *ACS Energy Lett*, 2019, **4**, 1258–1259.

15 J. Park, J. Kim, H. S. Yun, M. J. Paik, E. Noh, H. J. Mun, M. G. Kim, T. J. Shin and S. Il Seok, *Nature 2023 616:7958*, 2023, **616**, 724–730.

16 X. Xu, G. Zhang, L. Yu, R. Li and Q. Peng, *Advanced Materials*, 2019, **31**, 1906045.

17 X. Xu, K. Fukuda, A. Karki, S. Park, H. Kimura, H. Jinno, N. Watanabe, S. Yamamoto, S. Shimomura, D. Kitazawa, T. Yokota, S. Umezu, T.-Q. Nguyen and T. Someya, *Proceedings of the National Academy of Sciences*, 2018, **115**, 4589–4594.

18 T. Maksudov, M. He, S. Doukas, M. I. Nugraha, B. Adilbekova, H. Faber, L. Luo, R. Zhou, O. M. Bakr, W. Ogieglo, I. Pinnau, G. T. Harrison, D. R. Naphade, Z. Ling, E. Lidorikis, S. Fatayer, M. Heeney, F. H. Isikgor and T. D. Anthopoulos, *Materials Science and Engineering: R: Reports*, 2024, **159**, 100802.

19 L. Zhu, M. Zhang, J. Xu, C. Li, J. Yan, G. Zhou, W. Zhong, T. Hao, J. Song, X. Xue, Z. Zhou, R. Zeng, H. Zhu, C. C. Chen, R. C. I. MacKenzie, Y. Zou, J. Nelson, Y. Zhang, Y. Sun and F. Liu, *Nature Materials 2022 21:6*, 2022, **21**, 656–663.

20 L. Zhu, A. P. Raman and S. Fan, *Proc Natl Acad Sci U S A*, 2015, **112**, 12282–7.

21 J.-W. Cho, S.-J. Park, S.-J. Park, Y.-B. Kim, K.-Y. Kim, D. Bae and S.-K. Kim, *ACS Photonics*, DOI:10.1021/acsphotonics.0c00837.

22 X. Cui, W. Ma, Y. Zheng, M. Luo, S. Han, X. Sun, L. Zhou and X. Wei, *Solar Energy*, 2022, **248**, 210–220.

23 S. Ahn, S. Ahn, J. H. Yun, D. H. Lee, S. Winter, S. Igari and K. Yoon, *Metrologia*, 2014, **51**, 139.

24 B. H. Hamadani and B. Dougherty, *Semiconductor Materials for Solar Photovoltaic Cells*, 2015, **218**, 229–245.

25 Solar Simulator Spectral Irradiance Data, https://www.newport.com/n/solar-simulator-spectral-irradiance-data?srsltid=AfmBOorpGJUlCU-MII37MPNzuJfBxY4GTqQhuQ9Q3Wp1LfCnrz0zPP_9, (accessed 28 February 2025).

26 SpectroRadiometers- Solar Measurement Systems - StellarNet, Inc., https://www.stellarnet.us/systems/spectroradiometers-solar-measurement-systems/, (accessed 28 February 2025).

27 K. Xiao, R. Lin, Q. Han, Y. Hou, Z. Qin, H. T. Nguyen, J. Wen, M. Wei, V. Yeddu, M. I. Saidaminov, Y. Gao, X. Luo, Y. Wang, H. Gao, C. Zhang, J. Xu, J. Zhu, E. H. Sargent and H. Tan, *Nature Energy 2020 5:11*, 2020, **5**, 870–880.

28 C. Sun, R. Xia, H. Shi, H. Yao, X. Liu, J. Hou, F. Huang, H. L. Yip and Y. Cao, *Joule*, 2018, **2**, 1816–1826.

29 Y. Lin, Y. Firdaus, F. H. Isikgor, M. I. Nugraha, E. Yengel, G. T. Harrison, R. Hallani, A. El-Labban, H. Faber, C. Ma, X. Zheng, A. Subbiah, C. T. Howells, O. M. Bakr, I. McCulloch, S. De Wolf, L. Tsetseris and T. D. Anthopoulos, *ACS Energy Lett*, 2020, **5**, 2935–2944.

30 M. Zhang, B. Wilkinson, Y. Liao, J. Zheng, C. F. J. Lau, J. Kim, J. Bing, M. A. Green, S. Huang and A. W. Y. Ho-Baillie, *Joule*, 2018, **2**, 2694–2705.

31 Y. Jiang, I. Almansouri, S. Huang, T. Young, Y. Li, Y. Peng, Q. Hou, L. Spiccia, U. Bach, Y. B. Cheng, M. A. Green and A. Ho-Baillie, *J Mater Chem C Mater*, 2016, **4**, 5679–5689.

32 A. Reale, F. Michelotti, T. M. Brown, A. Di Carlo and L. Dominici, *Optics Express, Vol. 17, Issue 12, pp. 10155-10167*, 2009, **17**, 10155–10167.

33 F. Xu, F. Wang, S. Lei, J. Ou and W. Li, *Appl Phys A Mater Sci Process*, 2023, **129**, 1–10.

34 J. Mandal, Y. Fu, A. C. Overvig, M. Jia, K. Sun, N. N. Shi, H. Zhou, X. Xiao, N. Yu and Y. Yang, *Science (1979)*, 2018, **362**, 315–319.

35 M. Rubin, *Solar Energy Materials*, 1985, **12**, 275–288.

36 Y. Bormashenko, R. Pogreb, O. Stanevsky and E. Bormashenko, *Polym Test*, 2004, **23**, 791–796.

37 M. Dong, X. Zhao, Z. Chen, N. Chen and S. Fan, *Optics Express, Vol. 27, Issue 22, pp. 31587-31598*, 2019, **27**, 31587–31598.